Journal of Physics: Conference Series **756** (2016) 012005 doi:10.1088/1742-6596/756/1/012005

Multispectral Electrical Impedance Tomography using Optimization over Manifolds

A Fouchard[1,2], **S. Bonnet**[1], **O. David**[2]
[1]Université Grenoble Alpes, CEA, Leti, MINATEC Campus, 17 rue des Martyrs, F38054 Grenoble, Cedex 9, France
[2]Université Grenoble Alpes, Grenoble Institute of Neuroscience, Bâtiment E.J. Safra, Chemin Fortuné Ferrini, F38700 La Tronche, France

E-mail: alexandre.fouchard@centraliens-lyon.net

Abstract. Electrical impedance tomography under spectral constraints uses a material basis decomposition to combine the different information embedded in the tissue spectra. This approach offers an alternative to static imaging while benefiting from systemic error cancellation using difference data. It suits well cases where no prior solution is known and the contrast lies entirely between frequencies, e.g. to diagnose acute stroke or cancer. In this work, a computational framework is presented to deal with the extra frequency dimensions and the constraints during reconstruction. A fraction volume approach is demonstrated with explicit Euclidean gradient, usage of a finite volume element solver and minimization over the oblique manifold. It is applied to synthetic data. Parameter estimations are compared between a mono-frequency inversion and the proposed multispectral implementation. Results suggest that the proposed workflow enables to reduce the computational workload of multispectral inversion while ensuring valid proportions of materials within each control volume.

1. Introduction

Medical electrical impedance tomography (EIT) is a soft-field, non-invasive imaging technique. The setting of EIT consists in reconstructing internal electrical property distributions (conductivity σ and permittivity ε) from current and voltage boundary measurements at specific frequencies ω. The ill-posed EIT inverse problem limits the applications of static imaging, i.e. the deduction of quantitative conductivity maps. Besides, most EIT clinical applications currently use time difference imaging (tdEIT), e.g. in continuous pulmonary and brain function monitoring. It assumes variations of the conductivity distribution along with time, and estimates the parameter changes between two states [1].

The spectral signature of materials may also be used as a source of contrast in frequency difference imaging (fdEIT). This scheme could allow for the imaging without knowledge of a prior condition. It opens application areas in acute stroke, brain injury and cancer screening. However, while tdEIT enables systematic artefact reduction, fdEIT still suffers from strong noise amplification and cannot cope with modelling errors. This significantly reduces the fdEIT range of application [2].

To include frequency information in the image reconstruction process, spectrally constrained EIT (scEIT) has recently been introduced [3]. scEIT then stands as an alternative to static EIT while featuring the advantages of difference imaging techniques. The aim is to reduce the ill-conditioning of the inverse problem. scEIT makes use of a material basis decomposition: the conductivity of a control

volume is a linear combination of known tissue conductivities. The reconstruction then focuses on the proportion values of individual tissues within the imaging domain.

Since material proportions are frequency independent, multi-frequency data can be used directly. This contributes to reducing the degrees of freedom of the inversion problem, as long as the number of frequencies exceeds the number of tissues. Further, the knowledge of the tissue spectra enables using difference data in the objective function. Modelling and frequency independent instrumentation errors are mitigated in a nonlinear reconstruction scheme.

The drawbacks of the present approach is the computational workload. The iterative nonlinear inversion workflow involves solving the forward problem, calculating the multi-frequency Jacobian matrix and computing the update step several times. Constraints over proportions have also to be taken into account: they are positive and sum to one for each control volume.

In order to optimize the scEIT imaging method, we propose here a numerical framework based on the joint use of a finite volume element (FVE) forward solver and an optimization on a manifold for the quantitative parameter estimation. FVE brings a model reduction capability compared to finite element methods (FEM) without loss of information [4]. Further, the minimization of the objective function is performed over the oblique manifold to efficiently handle the constraints over proportions [5]. This approach standardizes the integration of spectral constraints. It offers a way to reduce the computational complexity of multi-frequency imaging.

Once the notations of the proportion mixing and the cost functions are fixed, the explicit Euclidean gradient is derived. The methodology of the minimization of the cost function over the oblique manifold is then detailed. Reconstructions over synthetic data are compared between mono-frequency static imaging and the proposed multispectral workflow.

2. Methods

2.1. Material basis: proportion mixing

The parameter estimation under special constraints considers the medium as a mixing model: (i) it is composed of a known number of tissues $t = 1 \dots T$; (ii) the conductivity spectrum s of each tissue is assumed to be known at all frequencies $f = 0 \dots N_f$ of measurements: $s_{ft} = \sigma(\omega_f, t)$; (iii) the conductivity of the kth control volume $k = 1 \dots N$ is fixed by a linear combination of the proportions p_{kt} of the different components, equation (1).

$$\sigma_k(\omega_f) = \sum_t p_{kt} s_{ft} \quad s.t. \quad \begin{matrix} 0 \le p_{kt} \le 1 \\ \sum_t p_{kt} = 1 \end{matrix} \tag{1}$$

Proportions of a tissue t are gathered under the vector $\mathbf{p}_t \in \mathbb{R}^{N\times 1}$ and considering all tissues in the matrix $\mathbf{P} = [\mathbf{p}_1 \dots \mathbf{p}_T] \in \mathbb{R}^{N\times T}$. In the same way, conductivities are gathered for a frequency f in the vector $\boldsymbol{\sigma}_f = \sigma(\omega_f) \in \mathbb{R}^{N\times 1}$ and in the matrix $\boldsymbol{\Sigma} = \left[\boldsymbol{\sigma}_0 \dots \boldsymbol{\sigma}_{N_f}\right] \in \mathbb{R}^{N\times(N_f+1)}$ for multi-frequency considerations. The mixing model of equation (1) is then expressed as $\boldsymbol{\Sigma} = \mathbf{P}\mathbf{S}^T$. The conductivity at a frequency f is deduced by $\boldsymbol{\sigma}_f = \mathbf{P}\mathbf{s}_{f:}$, with $\mathbf{S} = \left[\mathbf{s}_{0:}^T \dots \mathbf{s}_{N_f:}^T\right]^{\boldsymbol{T}} \in \mathbb{R}^{(N_f+1)\times T}$. Computing derivatives then makes use of the chain rule and includes the standard Jacobian matrix $\mathbf{J}$. For instance, the derivative of the predicted data, i.e. the computed measurements $\tilde{\mathbf{u}}$, relative to the proportions values: $\frac{\partial \tilde{\mathbf{u}}(\boldsymbol{\sigma}_f)}{\partial \mathbf{p}_t} = \frac{\partial \boldsymbol{\sigma}_f}{\partial \mathbf{p}_t}\frac{\partial \tilde{\mathbf{u}}(\boldsymbol{\sigma}_f)}{\partial \boldsymbol{\sigma}_f} = s_{ft}\mathbf{J}^T(\boldsymbol{\sigma}_f)$. In the following, $\mathbf{I}_n$, $\mathbf{0}_T$ and $\mathbf{1}_n$ denote respectively the identity matrix, the null vector, and the vector of ones of the specified dimension n.

2.2. Cost function

In scEIT, the cost function $\Phi(\mathbf{P})$ is expressed as the weighted sum of a data fit term $\Phi^{(df)}(\mathbf{P})$ and a spatial regularisation term $\Phi^{(r)}(\mathbf{P})$: $\Phi(\mathbf{P}) = \Phi^{(df)}(\mathbf{P}) + \alpha\Phi^{(r)}(\mathbf{P})$. α is a regularization parameter which balances the contribution of each term.

The data fit term $\Phi^{(df)}(\mathbf{P}) = \frac{1}{2}\sum_{f=1}^{N_f}\sum_{m=1}^{M} z_{mf}^2(\mathbf{P})$ is explained in equation (2). $\mathbf{u}(\omega_f)$ denotes the measured voltages at frequency ω_f over all source-detector configurations, indexed by $m = 1 \dots M$, and η a constant independent of proportions.

$$z_{mf} = \frac{\tilde{u}_m(\mathbf{Ps}_{f:}) - \tilde{u}_m(\mathbf{Ps}_{0:})}{\tilde{u}_m(\mathbf{Ps}_{0:})} - \frac{u_m(\omega_f) - u_m(\omega_0)}{u_m(\omega_0)} = \frac{\tilde{u}_m(\mathbf{Ps}_{f:})}{\tilde{u}_m(\mathbf{Ps}_{0:})} + \eta \tag{1}$$

The data fit term takes into account (i) the multi-frequency data, to increase the number of constraints and (ii) the normalized difference data, to reduce modelling and instrumentation errors. ω_0 is chosen as the reference frequency.

2.3. Explicit Euclidean gradient

The Euclidean gradient of the cost function is now derived explicitly.

Following the chain rule, $\frac{\partial \Phi^{(df)}}{\partial \mathbf{P}} = \sum_f \frac{\partial z_{mf}}{\partial \mathbf{P}} \frac{\partial \Phi^{(df)}}{\partial z_{mf}} = \sum_f \frac{\partial z_{mf}}{\partial \mathbf{P}} z_{mf}$. As a quotient derivative, the equation (3) holds, for each control volume k and tissue t.

$$\frac{\partial z_{mf}}{\partial p_{kt}} = \frac{[\mathbf{J}(\mathbf{Ps}_{f:})]_{mk} s_{ft} \tilde{u}_m(\mathbf{Ps}_{0:}) - \tilde{u}_m(\mathbf{Ps}_{f:})[\mathbf{J}(\mathbf{Ps}_{0:})]_{mk} s_{0t}}{u_m^2(\mathbf{Ps}_{0:})} \tag{3}$$

This translates into equation (4).

$$\left[\nabla \Phi^{(df)}(\mathbf{P})\right]_{tk} = \sum_f \sum_m \frac{[\mathbf{J}(\mathbf{Ps}_{f:})]_{mk} s_{ft} \tilde{u}_m(\mathbf{Ps}_{0:}) - \tilde{u}_m(\mathbf{Ps}_{f:})[\mathbf{J}(\mathbf{Ps}_{0:})]_{mk} s_{0t}}{u_m^2(\mathbf{Ps}_{0:})} z_{mf} \tag{4}$$

To simplify the understanding, the following notations are used: $F = N_f - 1$, $\mathbf{z} = \mathrm{vec}(\mathbf{Z}) \in \mathbb{R}^{MF\times 1}$ $\mathbf{s}^{(0)} \in \mathbb{R}^{1\times \mathrm{T}}$, $\mathbf{S}^{(1f)} \in \mathbb{R}^{F\times \mathrm{T}}$, i.e. $\mathbf{S}^{(1f)}$ contains the piled spectra for the frequencies indexed 1 to F participating to the reconstructions. $\mathbf{a} \in \mathbb{R}^{M\times 1}$, $\mathbf{b} \in \mathbb{R}^{MF\times 1}$, $\mathbf{J}^{(0)}$ and $\mathbf{J}^{(1f)}$ are defined by equation (5).

$$a_m = \frac{1}{\tilde{u}_m(\mathbf{Ps}_{0:})} \quad \mathbf{b} = \begin{bmatrix} \mathbf{b}^{(1)} \\ \vdots \\ \mathbf{b}^{(F)} \end{bmatrix} \quad b_m^{(f)} = \frac{\tilde{u}_m(\mathbf{Ps}_{f:})}{u_m^2(\mathbf{Ps}_{0:})} \tag{5}$$

$$\mathbf{J}^{(1f)} = \begin{bmatrix} \mathbf{J}^T(\mathbf{Ps}_{1:}) & \dots & \mathbf{J}^T(\mathbf{Ps}_{F:}) \end{bmatrix} \in \mathbb{R}^{N\times MF} \quad \mathbf{J}^{(0)} = \begin{bmatrix} \mathbf{J}^T(\mathbf{Ps}_{0:}) & \dots & \mathbf{J}^T(\mathbf{Ps}_{0:}) \end{bmatrix} \in \mathbb{R}^{N\times MF}$$

Using these notations, the Euclidean gradient can be written in a explicit form as in equation (6), which is suitable for implementation. $\otimes$ denotes the Kronecker product.

$$\nabla \Phi^{(df)}(\mathbf{P}) = \mathbf{J}^{(1f)} \mathrm{diag}(\mathbf{z}) \left[\mathbf{S}^{(1f)} \otimes \mathbf{a}\right] - \mathbf{J}^{(0)} \mathrm{diag}(\mathbf{z}) \left[\mathbf{s}^{(0)} \otimes \mathbf{b}\right] \tag{6}$$

2.4. Methodology of inversion under constraints

The cost function associated with the estimation of the proportions of the different components is nonlinear. An optimization over a manifold is used to estimate parameters while imposing the constraints on proportions.

2.4.1. Optimization on the oblique manifold The auxiliary variable $\boldsymbol{X} = \sqrt{\boldsymbol{P}^T} \in \mathbb{R}^{N\times T}$, i.e. $p_{kt} = x_{tk}^2$, is introduced. It translates the constraints on proportions into $\sum_t x_{tk}^2 = 1$. Following this change of variable, it amounts to an optimization under equality constraints, which is seamlessly handled by using the oblique manifold $\mathcal{M} = \mathcal{OB}(N_t, N_e) = \{\boldsymbol{X} \in \mathbb{R}^{N\times T} : (\boldsymbol{X}^T\boldsymbol{X})_{ii} = 1, i = 1{:}N\}$ (matrices with unitary column), also ensuring positivity of proportions.

The proportions can be directly estimated within the manifold $\mathcal{M}$. The Matlab® library Manopt, dedicated to manifold optimization, is used [6]. The Euclidean gradient of the objective function is projected onto $\mathcal{M}$, in order to determine the search direction and to evolve within $\mathcal{OB}$ using the concept of retractions.

Dedicated functions are implemented in Matlab® to provide the objective function and its Euclidean gradient, given an estimation of proportions. The chain rule enables deducing the gradient of the objective function relatively to the auxiliary variable $\mathbf{X}$: it translates into the Hadamard product of the Euclidean gradient by a factor $2\mathbf{X}^T$. The conjugate-gradient algorithm is then used to estimate the proportions for its efficiency, associated with an optimal line search at each iteration [6].

Regarding the implementation choices, a special care has to be taken for the algorithm initialization. The matrix proportions could be initialized with the first column equal to $\mathbf{p}_1 = \mathbf{1}_N$ (the background of the image) and the other set to $\mathbf{0}_N$. However, using the Manopt library and the change of variable would lead to a null gradient over all objective variables except $\mathbf{p}_1$: the algorithm would remain stuck in the vicinity of the initial point. We propose here to slightly shift from this point to allow for a correct evolution of the algorithm. The initial point is thus set to $\mathbf{p}_1 = 0.9999 * \mathbf{1}_N$ (background) and $\mathbf{p}_t = \frac{0.0001}{T-1} * \mathbf{1}_N \forall t \geq 2$ (other tissues). The associated medium then includes mostly the background and a small proportion of the mixing of all other identified components.

2.4.2. Markov Random Field spatial regularization As in [3], the ill-posed inverse problem is handled by a Markov random field (MRF), equation (7). $l(k)$ designates the neighbors of the control volume k. The objective is to constrain neighboring control volumes to have close proportion values. Such a regularization term provides robustness to noise while allowing a low computational time.

$$\Phi^{(r)}(\mathbf{P}) = \frac{1}{2}\sum_t \sum_k \sum_{l(k)} \left(p_{kt} - p_{l(k)t}\right)^2 \quad (7)$$

This term is efficiently computed using the Laplacian matrix $\mathbf{L}$ of the graph: $\Phi^{(r)}(\mathbf{P}) = (\mathrm{vec}(\mathbf{P})^T)(\mathbf{I}_T \otimes \mathbf{L})\mathrm{vec}(\mathbf{P})$. Its gradient is given by: $\nabla\Phi^{(r)}(\mathbf{P}) = 2\mathbf{L}\mathbf{P}$. The chain rule is then applied to deduce the derivative relatively to the auxiliary variable $\mathbf{X}$. The regularization parameter is deduced by the L-method [8]. The latter is applied on the residuals of the cost function data fit term according to the regularization parameter. The graph features two asymptotic lines. The abscissa of their intersection point is chosen as the optimal hyper-parameter.

2.5. FVE forward solver

The proportions are estimated using a FVE method [4,7]. The underlying idea is to shift the focus of the control volume from an elemental resolution to a nodal resolution. Compared to the initial FEM implementation in [3], this allows to reduce the number of control volumes N, e.g. in the study case by a factor 2, i.e. the ratio of the number of elements versus the number of nodes. This is of utmost importance, since the multi-frequency Jacobian computed at each iteration scales with $N \times MF$.

3. Results

A medium with two components – background and conductive inclusion – was considered, and their spectra were assumed known (Figure 1). Synthetic multispectral data was predicted by FEM on a 14 equally-spaced electrode 2D model. It used 15 frequencies, and a 2D forward mesh including 6,450 nodes. Reconstructions were performed using the same numerical phantom, and a different mesh, including 3,527 nodes corresponding to 6,713 elements.

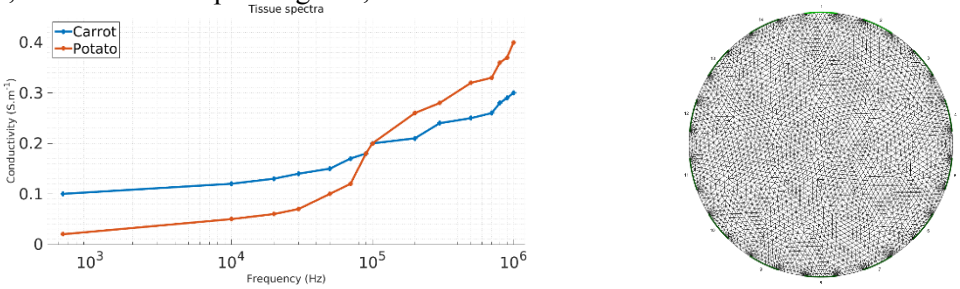

Figure 1. Conductivity spectra assumed known in the reconstruction - background: saline mixed with hashed carrots in blue, inclusion: potato in blue (left); inversion mesh with 14 electrodes (right).

Three situations were compared: (i) the parameter estimation using a mono-frequency nonlinear algorithm (Levenberg-Marquardt), (ii) the inversion through the proposed multispectral nonlinear scheme without spatial regularization, (iii) the deduction of proportions with the regularized multispectral framework together with the choice of an optimal regularization parameter. Conductivity maps and profiles were displayed for the results (the black circle indicated the expected position; the theoretical profiles were in red and the estimated ones in blue).

3.1. Mono-frequency reconstructions

Mono-frequency reconstructions led to estimated conductivity profiles that presented oscillations, due to the ill-posed behaviour of the inverse problem (Figure 2). The contrasts were relatively well recovered by the nonlinear inversion algorithm, relatively to the expected results.

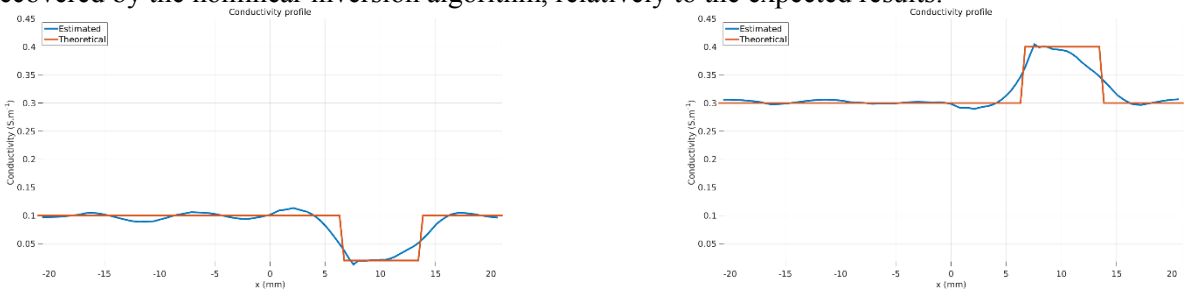

Figure 2. Conductivity profiles from mono-frequency nonlinear reconstructions at 640 Hz and 1 MHz.

3.2. Multispectral inversion using spectral constraints

The proportions of the different components were then estimated using the proposed scheme under spectral constraints. The multi-frequency data enabled to deduce proportion profiles that would no longer present oscillations, i.e. the ill-posed behaviour was reduced (Figure 3). Without spatial regularization, strong reconstruction artefacts were observed, namely in the vicinity of the centre of the numerical phantom. The MRF regularization tended to smooth the obtained profile, which approached the expected one.

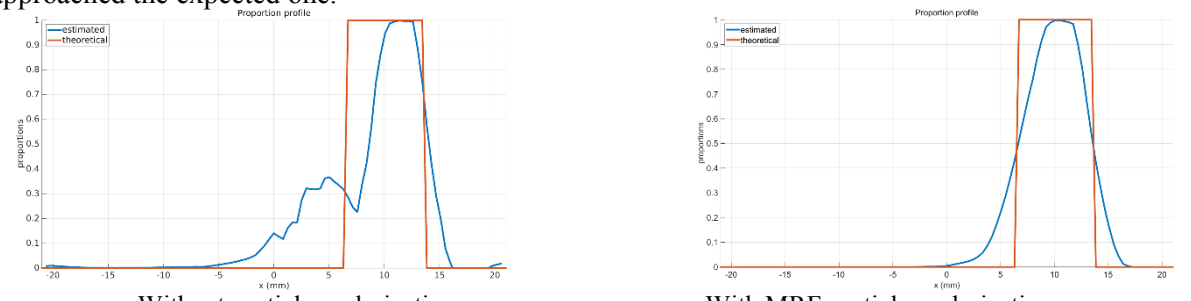

Without spatial regularization With MRF spatial regularization

Figure 3. Proportion profiles deduced by multispectral inversion (scEIT).

The inclusion of the spatial MRF regularization was then considered. Values of the hyper-parameter α were tried between 10^{-5} and 10^{-1} (Figure 4). For low values of α, artefacts were observed in the centre of the imaging domain, but the contrast in proportion was kept. For high values of α, the contrast was sharply inferior to the expected value, and artefacts tended to appear close to the boundary of the domain, with a spatial spread of the recovered proportions.

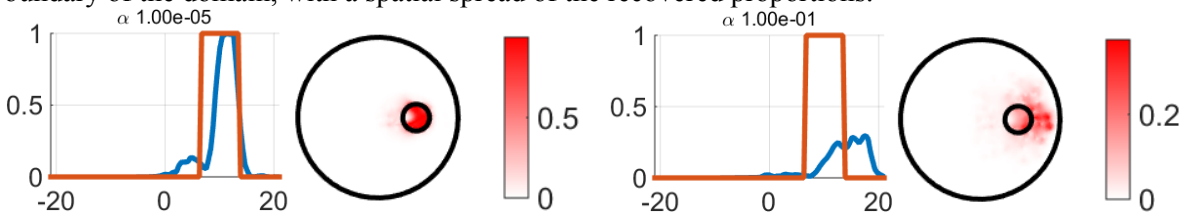

Figure 4. Proportion profiles and proportion maps of inclusion for extreme values of $\boldsymbol{\alpha}$.

Mono-frequency conductivity maps were then compared with spectrally constrained proportions (Figure 5). The former case showed that for some frequencies, the inclusion was not discernible; ringing effects were visible. The latter case showed a properly reconstructed inclusion: the spectral constraints allowed to feature very few artefacts and low ringing effects.

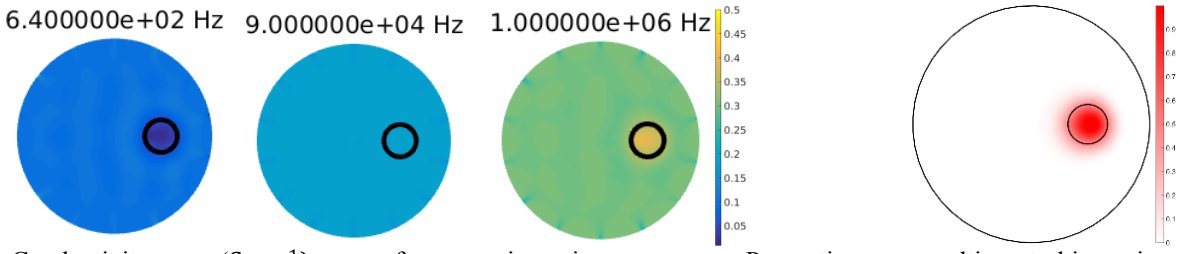

Conductivity maps ($S.m^{-1}$), mono-frequency inversion Proportion map, multispectral inversion

Figure 5. Estimated reconstructions from synthetic data.

4. Discussion

In this paper, we presented a numerical framework to handle the EIT multispectral inversion under spectral constraints. The multi-frequency Euclidean gradient was derived explicitly. Proportions were then estimated using the oblique manifold and a FVE solver (instead of standard FEM) to reduce the computational workload. The optimal regularization parameter was chosen using a bilinear regression.

Methods were tested on synthetic data. As expected, compared with a mono-frequency implementation, the quality of the multispectral reconstruction was enhanced. In this scope, the framework allowed to standardize the inversion workflow with the Manopt library. The minimization under equality constraints allowed ensuring valid proportions of materials at each control volume.

The proposed scEIT framework also enabled to enhance the efficiency of the inversion process, through the use of a FVE forward solver. With the 14 electrode phantom and the 15 frequencies used in this work, the size of the multi-frequency Jacobian that was computed at each iteration (20 iterations on average) was halved, translating into effective computation and assembly time savings. It would have valued in FEM $6{,}713 \times 14^2 * (15-1)$ elements versus $3{,}527 \times 14^2 * (15-1)$ in FVE.

Further studies will focus on applying these numerical developments to *in vitro* and *in vivo* data, with a straightforward extension to 3D and numerous tissues. They will also consider the robustness to the noise in the data and to the variations of the contact impedance at the medium-electrode junction.

References

[1] Holder D S (ed) 2004 *Electrical Impedance Tomography: Methods, History, and Applications* (London: Taylor & Francis)

[2] Seo J K and Woo E J 2013 Electrical impedance tomography *Nonlinear Inverse Problems in Imaging* (John Wiley & Sons, Ltd) 195–249

[3] Malone E, Sato dos Santos G, Holder D S and Arridge S 2014 Multifrequency electrical impedance tomography using spectral constraints *IEEE Trans. Med. Imaging* **33** 340–50

[4] Fouchard A, Bonnet S and David O 2015 Méthodes numériques pour le problème direct et l'analyse de sensibilité en tomographie d'impédance électrique *GRETSI* 2015 (Lyon, France)

[5] Absil P-A, Mahony R and Sepulchre R 2009 *Optimization Algorithms on Matrix Manifolds* (Princeton University Press)

[6] Boumal N, Mishra B, Absil P-A and Sepulchre R 2014 Manopt, a Matlab toolbox for optimization on manifolds *Journal. Mach. Learn. Res.* **15** 1455–9

[7] Fouchard A, Bonnet S, Hervé L and David O 2015 A current-density conservative nodal framework for EIT *International Conference on Biomedical Applications of Electrical Impedance Tomography* (Neûchatel, Suisse)

[8] Salvador S and Chan P 2004 Determining the number of clusters/segments in hierarchical clustering/segmentation algorithms *16th IEEE International Conference on Tools with Artificial Intelligence* 576–84 (Boca Raton, Florida, USA)